Electronic structure, noncollinear magnetism, and x-ray magnetic circular dichroism in the Mn_3ZnC perovskite

V. N. Antonov,[1,2] B. N. Harmon,[1] A. N. Yaresko,[3] and A. P. Shpak[2]
[1]*Ames Laboratory, Iowa State University, Ames, Iowa 50011, USA*
[2]*Institute of Metal Physics, 36 Vernadsky Street, 03142 Kiev, Ukraine*
[3]*Max Planck Institute for the Physics of Complex Systems, D-01187 Dresden, Germany*
(Received 4 December 2006; published 19 April 2007)

Mn_3ZnC possesses a magnetic phase transition at T_t=233 K from a ferromagnetic phase to a ferrimagnetic one with a noncollinear magnetic structure. The transition is accompanied by a structural change from cubic to tetragonal. The experimentally measured x-ray magnetic circular dichroism (XMCD) at the Mn *K* edge shows a drastic change at the magnetic phase transition, which is associated with the appearance of the noncollinear magnetic structure. The electronic structure and XMCD spectra of the Mn_3ZnC were investigated theoretically from first principles, using the fully relativistic Dirac linear muffin-tin orbital band-structure method for both the high-temperature cubic and low-temperature tetragonal noncollinear phases. Densities of valence states, spin, and orbital magnetic moments are analyzed and discussed. The origin of the XMCD spectra in the Mn_3ZnC compound is examined. The calculated results are compared with the experimental data.

DOI: 10.1103/PhysRevB.75.165114 PACS number(s): 75.50.Cc, 71.20.Lp, 71.15.Rf

I. INTRODUCTION

Ternary manganese compounds with the formula Mn_3MX (M=Ga, Sn, and Zn, and X=C and N) and the cubic crystal structure of perovskite type have attracted much interest due to their large variety of magnetic orderings and structural transformations.[1–9]

Mn_3GaC becomes a ferromagnet below T_c=255 K. Furthermore, as the temperature decreases from T_c, the first-order transition from a ferromagnet to an antiferromagnet, which involves a change of crystal structure from a cubic lattice to a rhombohedral one, has been observed at T_t =165 K.[10] The antiferromagnetic ordering below T_t is of the second kind, with an easy axis along the [111] direction. In the case of Mn_3SnC, the crystal structure is cubic in the whole temperature range and, below T_c=265 K, this compound becomes magnetic. The magnetic ordering was reported to be complex.[10]

In Mn_3ZnC, a magnetic phase transition occurs at T_t =233 K, which has been classified as a second-order transition from a ferromagnetic phase (T_c=380 K) to a ferrimagnetic one with a noncollinear magnetic structure.[8,9,11] The transition is accompanied by a structural change from cubic to tetragonal.

In these three compounds, the results of neutron diffraction show that the magnetic moments of Mn atoms are much smaller than the $4-5\mu_B$ observed in other ordered manganese alloys.[12] This result indicates a strong itinerant character of 3*d* electrons of Mn atoms in Mn_3MX. The observed paramagnetic susceptibility obeys the Curie-Weiss law with μ =$1.9\mu_B$ for Mn_3ZnC and μ=$2.41\mu_B$ for Mn_3GaC.[9] In the case of Mn_3SnC, the observed Curie-Weiss susceptibility has a slight upward convexity.[9]

The electronic structure of these compounds plays the key role in determining their magnetic and structural properties. The energy band structure of the Mn_3MX system has been calculated by various methods.[10,13–15] Jardin and Labbe[13] performed a band calculation of cubic perovskite compounds Mn_3MX by applying a simple tight-binding approximation to the *d* electrons of Mn atoms and *p* electrons of *X* atoms. They found a sharp singularity in the electronic density of states at the Fermi level and pointed out that the singularity of the density of states could explain the nature of the magnetic and structural phase transitions. In Ref. 10 the electronic bands of Mn_3ZnC, Mn_3GaC, Mn_3InC, and Mn_3SnC were calculated in the nonmagnetic state of the cubic perovskite structure by a self-consistent augmented-plane-wave method. The ferromagnetic bands of Mn_3GaC have also been calculated in cubic structure. The energy band structure of Mn_3GaC in nonmagnetic, ferromagnetic (FM), and antiferromagnetic (AFM) states was calculated using a self-consistent linearized augmented-plane-wave method in Ref. 14. It was found that the conduction bands around the Fermi level consist mainly of the Mn 3*d* orbitals which are not bonding with C 2*p* orbitals. Total energies for both the FM and AFM states were calculated as a function of the unit-cell volume.

In the present study, we focus our attention on the theoretical investigation of the x-ray magnetic circular dichroism in the low-temperature noncollinear phase of Mn_3ZnC. The x-ray magnetic circular dichroism (XMCD) technique developed in recent years has evolved into a powerful magnetometry tool to separate orbital and spin contributions to element-specific magnetic moments. XMCD experiments measure the absorption of x rays with opposite (left and right) states of circular polarization.

The 4*p* states in transition metals usually attract only minor interest because they are not the states constituting magnetic or orbital orders. Recently, however, understanding 4*p* states has become important since XMCD spectroscopy using *K* edges of transition metals became popular, in which the 1*s* core electrons are excited to the 4*p* states through the dipolar transition. The *K* edge XMCD is sensitive to electronic structures at neighboring sites because of the delocalized nature of the 4*p* states. Recently, in order to study the magnetic phase transition in Mn_3ZnC at 233 K, x-ray magnetic circular dichroism has been measured at the Mn *K* edge

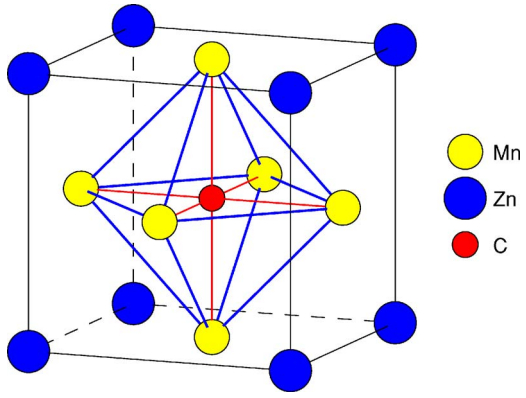

FIG. 1. (Color online) Cubic perovskite-type crystal structure of Mn_3ZnC at room temperature.

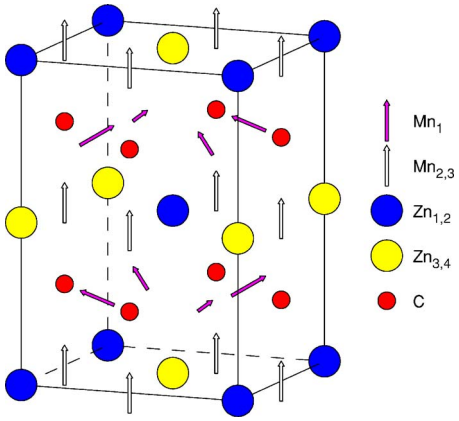

FIG. 2. (Color online) Low-temperature magnetic structure of Mn_3ZnC.

as a function of temperature and magnetic field.[16] When the transition appears, the spectral intensity of the prominent peak shows an abrupt drastic increase with decreasing temperature and a linear reduction with increasing magnetic field.

The theoretical investigations of the origin of the XMCD spectra at the K edges of Mn in the ferromagnetic cubic phases of Mn_3GaC and Mn_3ZnC have been carried out in Ref. 15 using the local spin-density approximation (LSDA). The origins of each structure have been analyzed in terms of orbital polarizations. However, there has been no systematic theoretical study of the electronic and magnetic structures as well as XMCD spectra in the low-temperature noncollinear Mn_3ZnC perovskite so far. The temperature- and magnetic-field-dependent XMCD still has to be explained from the theoretical point of view.

This paper is organized as follows. Section II presents a description of the perovskite Mn_3ZnC crystal and magnetic structures as well as the computational details. Section III is devoted to the electronic structure and XMCD spectra of the Mn_3ZnC compound calculated in the fully relativistic Dirac linear muffin-tin orbital (LMTO) band-structure method. The calculated results are compared with the available experimental data. Finally, the results are summarized in Sec. IV.

II. CRYSTAL STRUCTURE AND COMPUTATIONAL DETAILS

Mn_3ZnC at room temperature crystallizes in the cubic perovskite-type structure with $Pm\bar{3}m$ space group (No. 221), Mn atoms being at the face centers, Zn atoms at the corners, and C atoms at the body center (see Fig. 1). The Mn atoms have two carbon nearest neighbors at the 1.965 Å distance. The second coordination consists of eight Mn atoms and four Zn atoms at 2.779 Å.

A ferromagnetic to ferrimagnetic phase transition in Mn_3ZnC at T_t=233 K is accompanied by a structural change from cubic to tetragonal. The magnetic unit cell of the low-temperature ferrimagnetic phase ($P4\backslash mmm$ space group, No. 123) is composed of 4 f.u., and Mn ions form four layers and occupy three different sites:[8] Mn_1 possesses magnetic moments of $2.7\mu_B$ canting ±65° from the c axis to [111] direction, the Mn_2 and Mn_3 have magnetic moments of $1.67\mu_B$/Mn ferromagnetically aligned to the c axis (Fig. 2). Therefore, the Mn moments constitute a noncollinear magnetic structure.

In the low-temperature tetragonal structure, Mn-C interatomic distances are slightly decreased in comparison with the high-temperature cubic phase up to 1.958 Å. Mn_1 atoms are surrounded by two Mn_2 and two Mn_3 atoms at the 2.762 Å distance and four Mn_1 atoms at the 2.769 Å distance. Therefore, Mn-Mn interatomic distances are decreased through the cubic-tetragonal structure transition.

Within the one-particle approximation, the absorption coefficient μ for incident x rays is determined by the probability of electron transitions from an initial core state (with wave function ψ_j and energy E_j) to final unoccupied states (with wave functions $\psi_{n\mathbf{k}}$ and energies $E_{n\mathbf{k}}$) as

$$\mu_j^{\lambda}(\omega) = \sum_{n\mathbf{k}} |\langle \Psi_{n\mathbf{k}} | \mathcal{J}_{\lambda} | \Psi_j \rangle|^2 \delta(E_{n\mathbf{k}} - E_j - \hbar\omega)\,\theta(E_{n\mathbf{k}} - E_F), \tag{1}$$

where $\hbar\omega$ is the photon energy, λ its polarization, and $\mathcal{J}_{\lambda} = -e\mathbf{a}_{\lambda}$ being the dipole electron-photon interaction operator, where α are Dirac matrices and $\mathbf{a}_{\lambda}$ is the λ polarization unit vector of the photon vector potential $[a_{\pm} = 1/\sqrt{2}(1, \pm i, 0),\ a_z = (0,0,1)]$. (Here + and − denotes, respectively, left and right circular photon polarizations with respect to the magnetization direction in the solid.)

Concurrent with the development of the x-ray magnetic circular dichroism experiment, some important magneto-optical sum rules have been derived.[17–20]

For the K edges, the l_z sum rule was proposed in Ref. 21 and can be written as

$$\langle l_z \rangle = n_h \frac{2\int_K d\omega(\mu_+ - \mu_-)}{3\int_K d\omega(\mu_+ + \mu_-)}, \tag{2}$$

where $\langle l_z \rangle$ represents the expectation value of orbital angular momentum and n_h is the number of empty states per atom in

the $4p$ conduction bands. The integration is taken over the whole $1s$ absorption region.

The details of the computational method are described in our previous papers,[12,22] and here we only mention several aspects. The calculations were performed for the experimentally observed lattice constants ($a=3.930$ Å for the cubic perovskite-type structure, and $a=5.538$ Å and $c/a=1.407\,142$ for the low-temperature tetragonal phase) using the spin-polarized LMTO method,[23,24] with the combined correction term taken into account. We used the von Barth–Hedin parametrization[25] for the exchange-correlation potential. Brillouin zone integrations were performed using the improved tetrahedron method[26] and charge, self-consistently, was obtained with 405 irreducible **k** points. To improve the potential, we include additional empty spheres both in the cubic perovskite-type structure and in the low-temperature tetragonal phase. The basis consisted of Mn and Zn s, p, d, and f; C s, p, d, and empty spheres s; and p LMTOs.

The intrinsic broadening mechanisms have been accounted for by folding XMCD spectra with a Lorentzian. For the finite lifetime of the core hole, a constant width Γ_c, in general from Ref. 27, has been used. The finite apparative resolution of the spectrometer has been accounted for by a Gaussian of 0.6 eV.

In order to simplify the comparison of the theoretical x-ray isotropic absorption K spectra of Mn_3ZnC to the experimental ones, we take into account the background intensity which affects the high-energy part of the spectra and is caused by different kinds of inelastic scattering of the electron promoted to the conduction band above the Fermi level due to x-ray absorption (scattering on potentials of surrounding atoms, defects, phonons, etc.). To calculate the background spectra, we used the model proposed by Richtmyer *et al.*[28] (For details see Ref. 29.)

III. RESULTS AND DISCUSSION

A. Energy band structure

The total and partial densities of states (DOS) of cubic ferromagnetic Mn_3ZnC are presented in Fig. 3. The results agree well with previous band-structure calculations.[14] The occupied part of the valence band can be subdivided into several regions. C $2s$ states appear between -13.1 and -10.6 eV (not shown). Zn $3d$ states are fully occupied and cross the bottom of C $2p$ bands in a very narrow energy interval from -7.4 to -6.7 eV. C $2p$ states extended from -7 eV up to 15 eV. The states in the energy range -3.2–3.5 eV are formed by Mn d states. The crystal field at the Mn site (D_{4h} point symmetry) causes the splitting of d orbitals into three singlets a_{1g} and b_{1g} ($3z^2-1$ and x^2-y^2), b_{2g} (xz), and a doublet e_g (xy,yz). The $a_{1g}-b_g$ and $b_{2g}-e_g$ splittings are negligible in comparison with its width in LSDA calculations, therefore we present in Fig. 3 the DOS of "e_g" orbitals as a sum of the a_{1g} and b_{1g} ones and "t_{2g}" orbitals as a sum of the b_{2g} and e_g ones. One should mention that there is quite a small C $2p$-Mn d hybridization in the valence bands below the Fermi level.

Mn_3ZnC in cubic perovskite-type crystal structure has local magnetic moments of $2.362\mu_B$ on Mn, $-0.062\mu_B$ on Zn, and $-0.196\mu_B$ on C. The orbital moments are equal to $0.028\mu_B$, $0.001\mu_B$, and $0.0001\mu_B$ on the Mn, Zn and C sites, respectively. Our calculations produce a slightly larger spin magnetic moment at the Mn site in comparison with the Takahashi-Igarashi results ($2.176\mu_B$).[15] One of the possible reasons of such disagreement is the value of the atomic spheres. Takahashi and Igarashi used touching Muffin-tin spheres in the Korringa-Kohn-Rasbker scheme; however, we used larger atomic spheres in the atomic sphere approximation of the LMTO method, taking into account the combined correction terms.

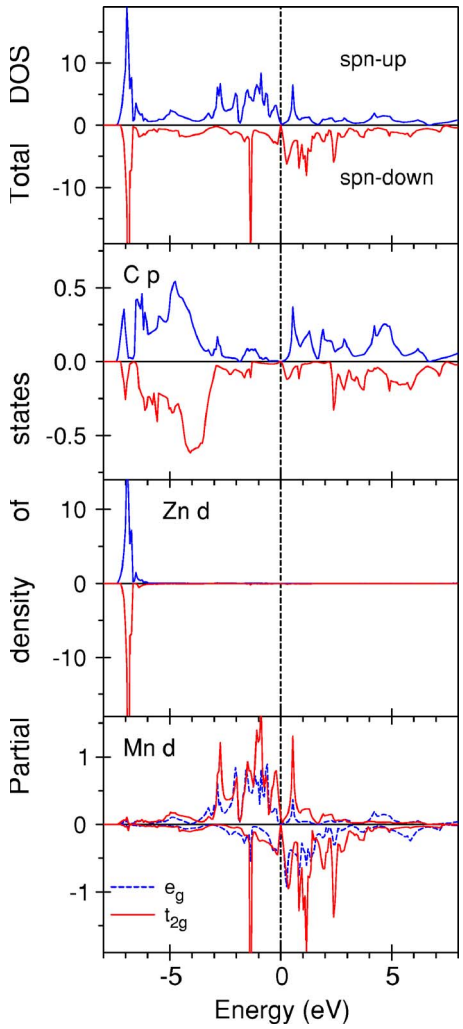

FIG. 3. (Color online) The total [in states/(cell eV)] and partial [in states/(atom eV)] ferromagnetic density of states of Mn_3ZnC in cubic perovskite-type structure. The Fermi energy is at zero.

Mn_3ZnC partial DOSs for the low-temperature tetragonal structure are presented in Fig. 4. For this crystal structure, spin magnetic moments are $2.269\mu_B$ on noncollinear Mn_1 atom sites, $1.956\mu_B$ on collinear $Mn_{2,3}$ ones, $-0.041\mu_B$ on Zn, and $-0.114\mu_B$ on C sites. The orbital moments are equal to -0.022, 0.009, -0.002, and $-0.002\mu_B$ on the Mn_1, $Mn_{2,3}$, Zn, and C sites, respectively.

The corresponding experimental spin magnetic moments are equal to $2.7\pm0.1\mu_B$ for Mn_1 atom sites and $1.6\pm0.1\mu_B$ for $Mn_{2,3}$ collinear sites.[8] One of the reasons for the dis-

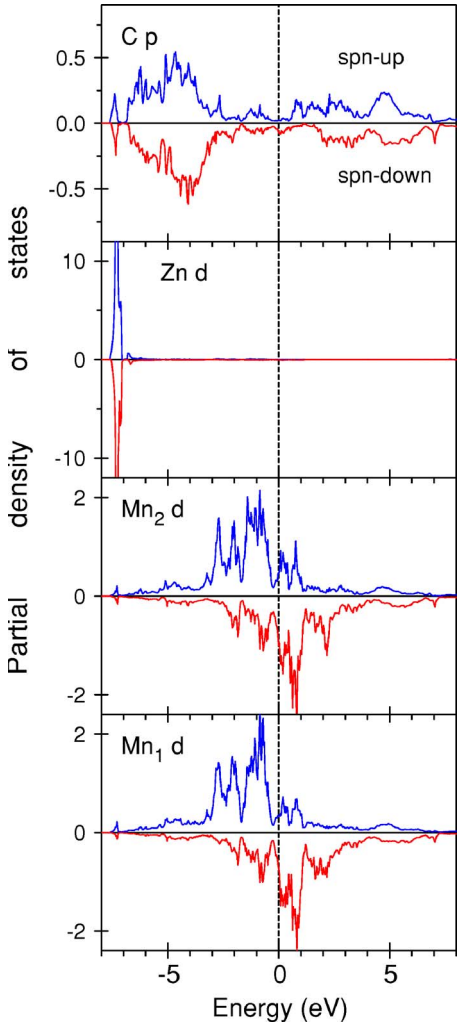

FIG. 4. (Color online) Partial density of states [in states/(atom eV)] of Mn_3ZnC in low-temperature noncollinear tetragonal structure. The Fermi energy is at zero.

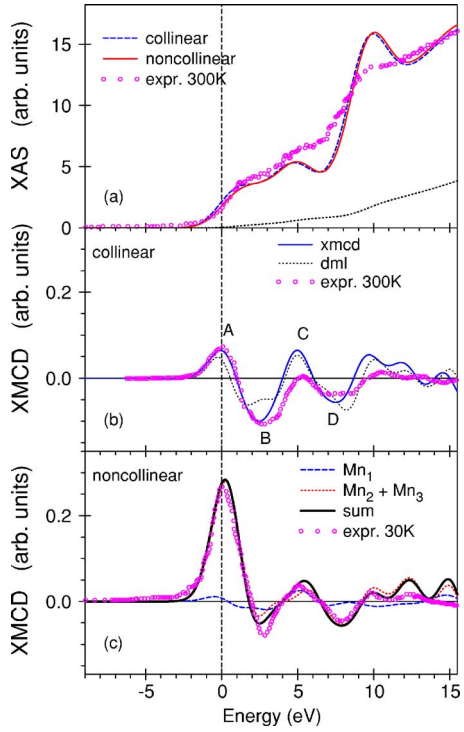

FIG. 5. (Color online) (a) Theoretically calculated isotropic absorption spectra of Mn_3ZnC at the Mn K edge for cubic high-temperature phase (dashed line) and low-temperature tetragonal structure (full line) in comparison with the experimental spectrum (Ref. 16) (circles) measured at 300 K. The dotted line shows the theoretically calculated background spectrum. (b) The experimental XMCD spectrum (Ref. 16) measured at 300 K (circles) and theoretically calculated XMCD spectra for cubic high-temperature phase (full line); the dotted line presents the $dm_{l=1}(E)$ function (see the explanation in the text), (c) Theoretically calculated XMCD spectrum for low-temperature tetragonal structure in comparison with the experimental measurements at 30 K (Ref. 16) (circles). Dashed and dotted lines show the theoretically calculated contributions from Mn_1 and Mn_2+Mn_3 sites, respectively; the thick full line is the total spectrum.

agreement between the theoretically calculated and experimental data may be possible intersite disorder.[30]

Total energy calculations show that the low-temperature tetragonal phase has higher energy in comparison with the cubic structure. The calculated exchange constants were found to be of ferromagnetic type for both the first and second neighbors. It raises the question of what stabilizes the low-temperature noncollinear structure. One should mention that, in fact, the low-temperature phase of Mn_3ZnC has not been refined yet. There are no experimentally obtained atomic positions in the low-temperature phase. In our calculations, we used an ideal tetragonal crystal structure calculated from the cubic phase $(a\sqrt{2}, a\sqrt{2}, 2c)$,[8] with $a=3.916$ Å.[16] Possible atomic shifts from ideal positions in the real structure may stabilize the low-temperature tetragonal noncollinear structure. Small atomic shifts will not affect strongly the XMCD spectra; however, it can influence the total energy value. The crystal structure of the low-temperature phase of Mn_3ZnC needs additional experimental investigation.

B. XMCD spectra

1. High-temperature cubic phase

Figure 5 shows the theoretically calculated Mn K-edge x-ray absorption spectra (XAS) as well as XMCD spectra in terms of the difference in absorption $\Delta\mu_K=\mu_K^+-\mu_K^-$ for left and right circularly polarized radiations in Mn_3ZnC in comparison with the corresponding experimental data.[16] In order to compare relative amplitudes of the K XMCD spectra, we first normalize the theoretically calculated x-ray absorption spectra to the experimental ones by taking into account the background scattering intensity[28] [Fig. 5(a)]. There are no large differences in the shape of XAS for low- and high-temperature phases of Mn_3ZnC, in agreement with the experimental measurements which show no significant temperature variation of XAS.[16] The experimental x-ray absorption spectra have three humps around 1.5, 5, and 10 eV above the Fermi level, which are well reproduced by the theoretical calculations.

Figure 5(b) shows the experimental XMCD spectrum[16] measured at 300 K and the theoretically calculated one using the LSDA for the cubic high-temperature phase. The theory is in good agreement with previous calculations[15] and the experimental measurements, although the calculated magnetic dichroism is somewhat too high at the 5 eV (peak *C*) and in the 9–13 eV energy range.

The 4*p*-3*d* hybridization and the spin-orbit interaction (SOI) in the 4*p* states play a crucial role for the *K*-edge dichroism. Actually, XMCD *K* spectrum reflects the orbital polarization in differential form $d\langle l_z\rangle/dE$ of the *p* states.[31,32] We calculated the site-dependent function $dm_{tl}(E) = \Sigma_{n\mathbf{k}}\langle\Psi_{tl}^{n\mathbf{k}}|\hat{l}_z|\Psi_{tl}^{n\mathbf{k}}\rangle\delta(E-E_{n\mathbf{k}})$,[33] where $\hat{l}_z$ is the *z* projection of the angular momentum operator, and $E_{n\mathbf{k}}$ and $\Psi_{tl}^{n\mathbf{k}}$ are the energy of the *n*th band and the part of the corresponding LMTO wave function formed by the states with the angular momentum *l* inside the atomic sphere centered at the site *t*, respectively. In analogy to the *l*-projected density of states, $dm_{tl}(E)$ can be referred to as the site- and *l*-projected densities of the expectation value of $\hat{l}_z$. This quantity has purely relativistic origins and when the SO interaction is equal to zero, $dm_{tl}(E) \equiv 0$. The orbital moment M_l at the site *t* is given by $M_{tl}(E) = \int_{E_b}^{E_F} dm_{tl}(E)dE$, where E_b is the bottom of the valence band. As can be seen in Fig. 5(b), the *K* XMCD spectrum and $dm_{tl}(E)$ function are indeed closely related to one another, giving a rather simple and straightforward interpretation of the XMCD spectra at the *K* edge.

The *K* XMCD spectra come from the orbital polarization in the empty *p* states, which may be induced by (1) the spin polarization in the *p* states through the SOI and (2) the orbital polarization at neighboring sites through hybridization. We calculated the XMCD spectra at Mn sites in the ferromagnetic cubic phase of Mn_3ZnC by turning the SOI off separately on the Mn 4*p* states and the Mn 3*d* states, respectively. We found that when the SOI on the Mn 3*d* states is turned off, the spectrum above 3.5 eV does not change, while the negative peak *B* is reduced and the prominent peak near the *K* edge (peak *A*) is largely diminished. On the other hand, when the SOI on the Mn 4*p* orbital is turned off, peaks *A* and *B* keep a similar shape, while peak *C* is reduced in intensity and the minimum *D* almost vanishes. We can conclude that the 3*d* orbital polarization at neighboring Mn sites induces the *p* orbital polarization near the edge through the 4*p*-3*d* hybridization. The spectrum at $\geqslant$3.5 eV above the Fermi level originates from the spin polarization in the 4*p* symmetric states through the SOI. Similar results have been obtained by Takahashi and Igarashi in the ferromagnetic cubic phases of Mn_3GaC.[15]

2. Low-temperature tetragonal phase

The experimental Mn *K* XMCD spectrum shows a noteworthy variation with temperature.[16] As the temperature is decreased, the dichroic intensity of peak *A* is rapidly increased, with other peaks being almost unaffected. When the positive peak *A* overcomes the negative contribution of peaks *B*, *C*, and *D*, the value of 4*p* orbital magnetic moment M_L^p indicates a reversal of sign from positive to negative around 185 K. The change in orbital moment is obviously associated with the appearance of the noncollinear magnetic structure.

Figure 5(c) presents the calculated XMCD spectra for low-temperature tetragonal Mn_3ZnC compound at the Mn *K* edges compared with the experimental data.[16] Although the number of Mn_1 atoms which are canting ±65° from the *c* axis to [111] direction is two times larger than the number of ferromagnetically aligned Mn_2 and Mn_3 atoms (Fig. 2), the main contribution to the prominent peak *A* situated near the Fermi edge comes from the $Mn_{2,3}$ atoms [Fig. 5(c)]. We found that $dm_{l=1}(E)$ function is three times larger at the $Mn_{2,3}$ sites than at Mn_1 around the Fermi edge. The orbital magnetic moment in *p*-projected DOS is equal to $-0.000\,10\mu_B$ at Mn_1 and $-0.001\,02\mu_B$ at the $Mn_{2,3}$ sites. Therefore the effect of SO coupling in 4*p* states is different for particular Mn sites in Mn_3ZnC.

To estimate the Mn orbital moment in the *p*-projected states, Maruyamaa *et al.*[16] integrated the experimental XMCD spectrum over the range of −5 eV–13 eV. The integrated XMCD intensity has a positive value in the tetragonal ferrimagnetic phase, which signifies a negative orbital magnetic moment in the *p*-projected bands by the relation $M_L = -\langle l_z\rangle\mu_B$. On the assumption of $n_h = 6$, the magnitude of M_L^p was estimated to be around $-0.000\,75\mu_B$/Mn from the sum rules [Eq. (2)].

We apply sum rules to our theoretically calculated XMCD spectra and obtained $M_L^p = -0.000\,12$ and $-0.001\,36\mu_B$ for the Mn_1 and $Mn_{2,3}$ sites, respectively, which gives the value of the $M_L^p = -0.000\,54\mu_B$/Mn in reasonable agreement with the experimental estimations and band-structure calculations.

We found that the $dm_{l=1}(E)$ function is 1.5 times larger at the $Mn_{2,3}$ sites than at the Mn site in the cubic high-temperature phase around the Fermi edge. Besides, due to lowering crystal symmetry from cubic to tetragonal through structural phase transition and decreasing Mn-Mn interatomic distances, the 4*p*-3*d* hybridization is increased. It affects mostly the states near the Fermi edge because the Mn *d* DOS are rather small at $\geqslant$3.5 eV above the Fermi level (Fig. 4); therefore, the main changes of the intensity of the dichroic signal due to this effect would be expected at the prominent peak *A* [Fig. 5(c)].

We can conclude that the increase of the 4*p*-3*d* hybridization and the change of the effect of SO coupling in the 4*p* states lead to a strong increase of the spectral intensity of the prominent peak *A* through structural and magnetic phase transitions at $T_t = 233$ K.

Maruyamaa *et al.*[16] measured the magnetic-field variation of the dichroic spectrum and found surprising results: peaks *B* and *D* are sensitive and increase with negative intensity, whereas peak *A* is rather insensitive to the applied magnetic field (just slightly increases with increasing magnetic field from 0.5 to 10 T). Therefore the dichroic spectral peak makes a different response to the external parameters; roughly, peak *A* is sensitive to temperature, while the other peaks are sensitive to magnetic field. The authors speculate that this behavior indicates a process in which the canted Mn orbital moments are forced to align to the direction of applied magnetic field.

We investigated the influence of the Mn_1 canting angle on the XMCD spectra and 4*p* orbital magnetic moments at Mn

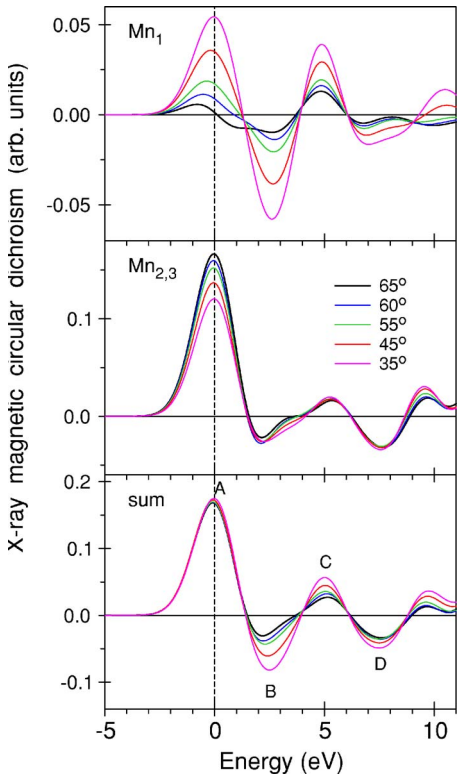

FIG. 6. (Color online) Theoretically calculated XMCD spectra at the Mn_1 and $Mn_{2,3}$ sites as a function of the canted Mn_1 angle for low-temperature tetragonal structure.

sites. Figure 6 presents the theoretically calculated XMCD spectra at the Mn_1 and $Mn_{2,3}$ sites as a function of the Mn_1 canting angle for the low-temperature tetragonal structure. We found that the prominent peak *A* is rather insensitive to the Mn_1 canting in the 65°–35° angle interval. On the other hand, peak *B* strongly increased in the same angle range. It can be explained by the different behaviors of these peaks at the Mn_1 and $Mn_{2,3}$ sites. By decreasing the canting angle, the intensity of peak *A* is increased at the Mn_1 site and decreased at the $Mn_{2,3}$ sites, almost compensating for each other. However, peak *B* increased at both nonequivalent sites, with an especially strong increase at the Mn_1 site. We found a similar behavior also for the function $dm_{l=1}(E)$ (not shown).

Figure 7 presents the variation of Mn $4p$ orbital moments at the Mn_1 and $Mn_{2,3}$ sites with the canting Mn_1 angle. Both the orbital moments are negative for most of the angle interval. The $Mn_{2,3}$ $4p$ orbital moments are slightly decreased when canting angle changes from 65° to 40°, and more quickly decrease with further decrease of the canting angle. On the other hand, the Mn_1 $4p$ orbital moment is first increased from 65° to 40° and then decreased. As the canting Mn_1 angle is decreased further, the value of M_L^p indicated a reversal of sign from negative to positive around 15° and 7° for the Mn_1 and $Mn_{2,3}$ sites, respectively, which is responsible for the trend that the negative peaks *B* and *D* overcome the positive contribution of peaks *A* and *C*.

IV. SUMMARY

In Mn_3ZnC, a magnetic phase transition occurs at $T_t = 233$ K, which has been classified as a second-order transition from a ferromagnetic phase to a ferrimagnetic one with a noncollinear magnetic structure. The transition is accompanied by a structural change from cubic to tetragonal. The experimental Mn *K* XMCD spectrum shows a noteworthy variation with temperature. As the temperature is decreased, the dichroic intensity of peak *A* is rapidly increased, with other peaks being almost unaffected. On the other hand, peak *A* is rather insensitive to the applied magnetic field, but the negative peaks *B* and *D* significantly increased with negative intensity with increasing magnetic field.

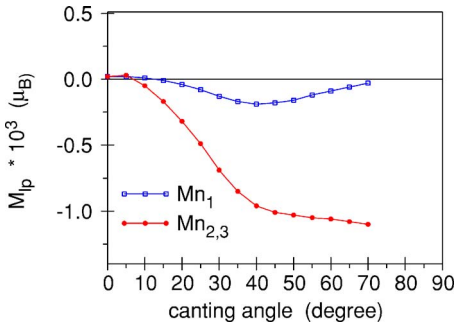

FIG. 7. (Color online) Variation of Mn $4p$ orbital moments at the Mn_1 and $Mn_{2,3}$ sites with the canted Mn_1 angle.

We have studied the electronic structure and x-ray magnetic circular dichroism spectra in the ferromagnetic and low-temperature noncollinear phases of Mn_3ZnC perovskite compound in the LSDA by means of an *ab initio* fully relativistic spin-polarized Dirac linear muffin-tin orbital method. The calculated spectra show excellent agreement with the experiment. We found that the increase of the $4p$-$3d$ hybridization and change of the effect of SO coupling in the $4p$ states lead to the drastic increase of the spectral intensity of the prominent peak *A* through structural and magnetic phase transitions at $T_t = 233$ K.

To model the influence of the external magnetic field on the XMCD spectra of low-temperature Mn_3ZnC perovskite, we investigated the influence of the Mn_1 canting angle on the XMCD spectra and $4p$ orbital magnetic moment at Mn sites. We found that the prominent peak *A* is rather insensitive to the Mn_1 canting angle when the canting angle changes from 65° to 35°. On the other hand, peak *B* strongly increases in the same angle interval. The variation of Mn $4p$ orbital moments at the Mn_1 and $Mn_{2,3}$ sites with the canting Mn_1 angle show that both the orbital moments are negative for most of the angle interval, which is responsible for the trend that the positive peaks *A* overcome the negative contribution of peaks *B* and *D*.

ACKNOWLEDGMENTS

This work was carried out at the Ames Laboratory, which is operated for the U.S. Department of Energy by Iowa State University under Contract No. DE-AC02-07CH11358. This work was supported by the Office of Basic Energy Sciences of the U.S. Department of Energy. V.N.A. gratefully acknowledges the hospitality at the Ames Laboratory during his stay.

[1] M. Guillot and R. P. Pauthenet, C. R. Acad. Sci. URSS **258**, 3242 (1964).
[2] J. P. Bouchaud and R. Fruchart, C. R. Acad. Sci. URSS **261**, 458 (1965).
[3] J. J. Pierre, J. P. Bouchaud, R. Fruchart, M. Guillot, H. Bartholin, and F. Chaissé, C. R. Acad. Sci. URSS **261**, 655 (1965).
[4] J. P. Bouchaud, R. Fruchart, P. Pauthenet, M. Guillot, H. Bartholin, and F. Chaissé, J. Appl. Phys. **37**, 971 (1966).
[5] D. Fruchart, E. F. Bertaut, F. Sayetat, M. N. Eddine, R. Fruchart, and J. P. Senateur, Solid State Commun. **8**, 91 (1970).
[6] A. Kenmotsu, T. Shinohara, and H. Watanabe, J. Phys. Soc. Jpn. **32**, 377 (1972).
[7] D. Fruchart, E. F. Bertaut, B. L. Clerc, L. D. Khoi, P. Veittet, G. Lorthioir, M. E. Fruchart, and R. Fruchart, J. Solid State Chem. **8**, 182 (1973).
[8] D. Fruchart and B. F. Bertaut, J. Phys. Soc. Jpn. **44**, 781 (1978).
[9] T. Kaneko, T. Kanomata, and K. Shirakawa, J. Phys. Soc. Jpn. **56**, 4047 (1987).
[10] K. Motizuki and H. Nagai, J. Phys. C **21**, 5251 (1988).
[11] T. Kanomata, T. Kawashima, H. Yoshida, and T. Kaneko, J. Appl. Phys. **67**, 4824 (1990).
[12] V. Antonov, B. Harmon, and A. Yaresko, *Electronic Structure and Magneto-Optical Properties of Solids* (Kluwer Academic, Dordrecht, 2004).
[13] J. P. Jardin and J. Labbe, J. Phys. (Paris) **36**, 1317 (1975).
[14] M. Shirai, Y. Ohata, N. Suzuki, and K. Motizuki, Jpn. J. Appl. Phys., Suppl. **32**, 250 (1993).
[15] M. Takahashi and J. I. Igarashi, Phys. Rev. B **67**, 245104 (2003).
[16] H. Maruyamaa, N. Ishimatsua, and N. Kawamurab, Physica B **351**, 328 (2004).
[17] B. T. Thole and G. van der Laan, Phys. Rev. B **38**, 3158 (1988).
[18] B. T. Thole, P. Carra, F. Sette, and G. van der Laan, Phys. Rev. Lett. **68**, 1943 (1992).
[19] P. Carra, B. T. Thole, M. Altarelli, and X. Wang, Phys. Rev. Lett. **70**, 694 (1993).
[20] G. van der Laan and B. T. Thole, Phys. Rev. B **53**, 14458 (1996).
[21] S. Uemoto, H. Maruyama, N. Kawamura, S. Uemura, N. Kitamoto, H. Nakao, S. Hara, M. Suzuki, D. Fruchart, and H. Yamazaki, J. Synchrotron Radiat. **8**, 449 (2001).
[22] V. N. Antonov, B. N. Harmon, and A. N. Yaresko, Phys. Rev. B **64**, 024402 (2001).
[23] O. K. Andersen, Phys. Rev. B **12**, 3060 (1975).
[24] V. V. Nemoshkalenko and V. N. Antonov, *Computational Methods in Solid State Physics* (Gordon and Breach Science, Amsterdam, 1998).
[25] U. von Barth and L. Hedin, J. Phys. C **5**, 1629 (1972).
[26] P. E. Blöchl, O. Jepsen, and O. K. Andersen, Phys. Rev. B **49**, 16223 (1994).
[27] J. C. Fuggle and J. E. Inglesfield, *Unoccupied Electronic States*, Topics in Applied Physics Vol. 69 (Springer, New York, 1992).
[28] F. K. Richtmyer, S. W. Barnes, and E. Ramberg, Phys. Rev. **46**, 843 (1934).
[29] V. N. Antonov, O. Jepsen, A. N. Yaresko, and A. P. Shpak, J. Appl. Phys. **100**, 043711 (2006).
[30] V. N. Antonov, B. N. Harmon, A. N. Yaresko, L. V. Bekenov, and A. P. Shpak, Phys. Rev. B **73**, 094445 (2006).
[31] H. J. Gotsis and P. Strange, J. Phys.: Condens. Matter **6**, 1409 (1994).
[32] M. S. S. Brooks and B. Johansson, in *Spin-Orbit Influenced Spectroscopies*, edited by H. Ebert and G. Schütz (Springer, Berlin, 1996), p. 211.
[33] L. Uba, S. Uba, V. N. Antonov, A. N. Yaresko, T. Slezak, and J. Korecki, Phys. Rev. B **62**, 13731 (2000).